Modeling, Identification and Control, Vol. 45, No. 1, 2024, pp. 29–39, ISSN 1890–1328

On the Necessity of Inflow Dynamics

F. Matras [1] M. D. Pedersen [1]

[1] *Department of Engineering Cybernetics, Norwegian University of Science and Technology, N-7491 Trondheim, Norway. E-mail:* {finn.matras,morten.d.pedersen}@ntnu.no

Abstract

This work explores the importance of dynamic inflow for wind turbines of varying rotor radius and also includes various coplanar multirotor setups. A parametrized model including the rotor and inflow dynamics is formulated. Typical values and ranges for the parameters are estimated using theoretical results and empirical data. The model is analyzed in terms of the kinetic energy and its dynamic responses. By analyzing the ratio of kinetic energy in the rotor vs. induced flow, we obtain a scalar measure for the relative importance of the dynamic inflow. Furthermore, the linearized closed-loop dynamics of a wind turbine around its optimum are examined in terms of the eigenvalues and time constants. This gives insights into the stability and control requirements for wind turbine systems. The results show that dynamic inflow should be included in wind turbine modeling and control of most wind turbines, and can only be ignored for small isolated rotors.

Keywords: scaling, eigenvalues, time constants, wind turbine

1 Introduction

There is an ongoing expansion in global wind energy which is expected to increase in the coming years, Hutchinson and Zhao (2023), reflecting its vital role in global energy production. This growth highlights the importance of wind power for energy production. Despite the widespread adoption of wind turbines today, there are still engineering challenges that need to be overcome Veers et al. (2023). As wind energy technology evolves, overcoming these challenges should be one of the key focus areas.

A wind turbine's primary function is to convert kinetic energy in the wind into electric energy. This is done by first converting the kinetic energy from the wind into energy in the rotor, which then through the generator is converted to electric energy. During this process, energy is removed from the wind, slowing down the freestream wind as it passes the rotor. This reduction in wind velocity is referred to as the induced flow, or inflow.

Even though it is well known that the inflow is a dynamic phenomenon, most work on design, modeling and control is based on the assumption of static inflow, Pao and Johnson (2009). This subjects the turbines to higher loadings Odgaaard et al. (2015) and might result in a shorter lifetime. Further design, simulation and control issues arise when wind turbines are placed in an offshore setting, Bashetty and Ozcelik (2021).

The wind energy community has had an ongoing discussion about whether dynamic inflow modeling is required or not, Odgaaard et al. (2015). An investigation of the effect of dynamic wind speed estimation with and without dynamic inflow conducted in Henriksen et al. (2013) concluded that it should be included in state estimators and model-based control schemes. In fact, Papi et al. (2023) shows that a flow model with dynamic inflow has lower variations in induced flow, as it effectively acts as a low-pass filter.

While a significant proportion of previous work on wind turbine control has focused on maximizing energy capture, such as Johnson et al. (2006), these do not include the inflow dynamics. Some authors such as Henriksen et al. (2012) have included dynamic inflow

doi:10.4173/mic.2024.1.3

and concluded that it is important for good control implementations. Similarly, Odgaaard et al. (2015) investigated the use of dynamic inflow in Model Predictive Control (MPC) design and found that with the use of dynamic inflow the tower fatigue load could be significantly reduced while almost not influencing the produced energy. However, including inflow dynamics is only part of the challenge, various types of inflow models have varying influence on control and fatigue loads, Mancini et al. (2023).

While some previous work has evaluated the necessity of dynamic inflow in wind turbine systems, no previous work was found that could give a quantitative measure of how important dynamic inflow is, and how the importance of dynamic inflow changes with the rotor size or multirotor configurations. Most previous work is focused on large turbines in the category of the 5MW turbine presented by Jonkman et al. (2009). Additionally, the concept of multirotor wind turbines has resurfaced in recent years with various researchers investigating these concepts Zhang et al. (2022), but the effect of dynamic inflow on such systems is also underexplored.

The primary objective of this work is to analyze the necessity of dynamic inflow for varying rotor sizes and coplanar multirotor configurations. This will be done by:

- Quantitatively analyzing the ratio of kinetic energy in the rotor and inflow systems to determine their relative contribution at various radii and rotor counts.
- Formulating a simplified dynamic model on state space form for a wind turbine operating at its optimum and linearizing it.
- Analyzing the linearized dynamic model in terms of its eigenvalues and time constants for varying rotor radii and quantities.

While the model is developed for actuator disk rotors as a coplanar multirotor setup, it still models single-rotor wind turbines, as these can be seen as a special case of the multirotor setup. Worth noting is that only the rotor and inflow dynamics are considered. Other dynamic systems such as the tower and support structure dynamics are omitted and are assumed not to have a significant influence on the results presented herein.

2 Energy Modeling

We start the analysis by exploring where the energy in a rotor system is present. This approach allows us to easily highlight which system components are important, based on how much energy they contain. For this, we let the power factor η be the ratio between the kinetic energy contained in the inflow and the kinetic energy in the rotor. This is an advantageous approach since η is a scalar quantity and it is thus easy to interpret and compare.

2.1 Energy in the Rotors

The rotor dynamics of wind turbines are assumed to remain independent no matter how many rotors the wind turbine consists of. The kinetic energy of a system with N rotors is thus given as

$$E_r = \sum_{n=1}^{N} \frac{1}{2} J \omega_n^2 = \frac{1}{2} \boldsymbol{\omega}^\intercal \boldsymbol{J} \boldsymbol{\omega} = \frac{J}{2} \boldsymbol{\omega}^\intercal \boldsymbol{\omega}. \tag{1}$$

The vector $\boldsymbol{\omega}$ contains the rotational velocities of each rotor, while $\boldsymbol{J}$ is a diagonal matrix with the inertia of each rotor, J. For $N = 1$ we obtain the kinetic energy for the monorotor system.

2.1.1 Rotor Inertia Modeling

The rotor inertia J requires a parametrization in the rotor radius R for further analysis. As rotor systems have different blade designs based on their intended use cases and operational requirements, it is challenging to generalize the blades on a theoretical basis. In an aim to give a decent representation, we model the mass and inertia of wind turbine blades based on data from commercial wind turbines in the range from sub-one meter radius of Istabreeze (2023) to over sixty meters in the form of the well-known 5MW reference turbine presented by Jonkman et al. (2009).

Let the inertia of the blades be given by a cylinder of mass m with radius of gyration γ:

$$J_b = m(\gamma R)^2. \tag{2}$$

The total rotor blade mass, m, theoretically follows scaling laws that dictate that the mass of a turbine blade should grow with the radius R cubed, Canet et al. (2021). However, empirical data indicate a growth that is somewhat slower than this. We utilize the general model on the form

$$m = \kappa R^{3-\beta}, \tag{3}$$

with scaling factor κ and a correction factor β, representing the deviation from the theoretical scaling law.

In addition to the blades, the generator and hub also introduce an additional moment of inertia. As this value depends on the rated wind speed and general turbine design, we will assume it to be proportional to the blade inertia, as is done in Tang et al. (2008). The total rotor moment of inertia is thus given by

$$J = \sigma J_b = \sigma \kappa R^{3-\beta} (\gamma R)^2, \tag{4}$$

where σ is a nondimensional scaling parameter.

2.2 Energy in the Inflow

Modeling the energy contained in the inflow is a somewhat complex task. While there are various ways of accomplishing this, we utilize the assumptions of an inviscid, incompressible flow, with the flow field being described by a potential ϕ, such that the three-dimensional inflow is given by $\nabla\phi$. This approach has been widely used in the realm of inflow modeling as shown in Peters (2009).

Following Batchelor (1967), the kinetic energy of the induced axial flow, with density ρ through an actuator disk is given as

$$E_i = \frac{1}{2}\rho \int \boldsymbol{u}\cdot\boldsymbol{u}\ dV = \frac{1}{2}\rho \int_0^{2\pi}\int_0^{\infty} \phi \boldsymbol{u}\cdot\boldsymbol{n}\ dr\ d\theta, \quad (5)$$

where $\boldsymbol{n}$ is the axial unit vector. Furthermore, the potential ϕ of a uniformly loaded actuator disk experiencing an induced flow w with radius R is given in Conway (1995) as

$$\phi = wR\int_0^{\infty} \frac{J_1(sR)J_0(sR)}{s} ds, \quad (6)$$

where J_0 and J_1 are the first- and second-order Bessel functions of the first kind. An expression for the vertical flow $\boldsymbol{u}\cdot\boldsymbol{n}$ evaluated on the disk is also given in Conway (1995) and reads

$$\boldsymbol{u}\cdot\boldsymbol{n} = u_z = wR\int_0^{\infty} J_1(sR)J_0(sr) ds. \quad (7)$$

Inserting (7) and (6) into (5) and integrating, one finds the energy for a single rotor to be

$$E_i = \mu\rho\pi R^3 w^2, \quad (8)$$

with $\mu = \frac{8}{3\pi}$ being the virtual inertia of the induced flow.

The induced flow for a multirotor setup is more challenging to compute, as it has to include the aerodynamic coupling between the rotors. This can be done by shifting the potential given in (6) by the distance between the rotor centers, effectively evaluating the flow at a different rotor. While this can be challenging in the spatial domain, it is a trivial task in the frequency domain, thanks to the two-dimensional Fourier shift operator in polar coordinates

$$\exp\left(-i\delta Rk\cos(\theta-\Psi)\right). \quad (9)$$

Here, k and ψ are the polar frequency coordinates, and δ and θ are the shifts in polar coordinates, note that the shift is normalized with respect to the radius. We will utilize the two-dimensional Fourier transform given by

$$\hat{f}(k,\Psi) = \frac{1}{2\pi}\int_0^{\infty}\int_0^{2\pi} f(r,\psi)\exp(-ikr\cos(\Psi-\psi))r\ d\psi\ dr. \quad (10)$$

Computing the Fourier transforms of (6) and (7) gives

$$\hat{\phi} = \frac{RwJ_1(kR)}{k^2} \quad (11)$$

$$\hat{u}_z = \frac{RwJ_1(kR)}{k}. \quad (12)$$

Using Plancherel's theorem and inserting the shift operator, we can now compute the energy for the interaction between any two rotors on the plane using

$$E_i = \frac{\rho}{2}\int_0^{\infty}\int_0^{2\pi} \hat{\phi}\hat{u}_z \exp\left(-i\delta Rk\cos(\theta-\Psi)\right)k\ d\Psi\ dk. \quad (13)$$

Aggregating all induced flows for the N rotors into a vector $\boldsymbol{w} = [w_1, w_2, \cdots, w_N]^\top$, and all virtual inertias μ for all rotor pairs in a matrix $\boldsymbol{M}$, one can formulate the energy in matrix-vector form

$$E_i = \rho\pi R^3 \boldsymbol{w}^\intercal \boldsymbol{M}\boldsymbol{w}. \quad (14)$$

The matrix $\boldsymbol{M}$ is nondimensional and symmetric.

2.3 Rotor Coupling Example

To illustrate the above coupling between the rotors, we will now investigate an example with two rotors and look at how the spatial separation influences the coupling. Consider a system of two rotors with mass-matrix

$$\boldsymbol{M} = \frac{8}{3\pi}\begin{bmatrix} 1 & c(\delta) \\ c(\delta) & 1 \end{bmatrix}, \quad (15)$$

where $c(\delta)$ is the normalized coupling term as a function of the rotor distance, which can be computed using (13). When $\delta \to \infty$ the rotors become decoupled and we are left with a diagonal mass matrix describing a system with kinetic energy

$$E_i|_{\delta\to\infty} = \rho\pi R^3\mu(w_1^2 + w_2^2) = 2\rho\pi R^3\mu w^2, \quad (16)$$

where the induced flow on rotor 1, w_1, is assumed to be equal to the induced flow on rotor 2, w_2. The total virtual mass and kinetic energy of two decoupled systems is twice that of one system. In the opposite extreme, when $\delta \to 0$, the coupling between the rotors becomes as strong as their self influence, in other words $c(0) = 1$, and we get the energy

$$E_i|_{\delta\to 0} = \rho\pi R^3\mu(w_1^2 + 2w_1w_2 + w_2^2) = 2E_i|_{\delta\to\infty} \quad (17)$$

Now, the total virtual mass and kinetic energy is twice that of the two decoupled rotors, or four times that of one rotor. Figure 1 shows the effect of the rotor separation distance on the scaling of the virtual mass and kinetic energy. One can verify that the function tends to the appropriate limits and that there is a smooth transition between these.

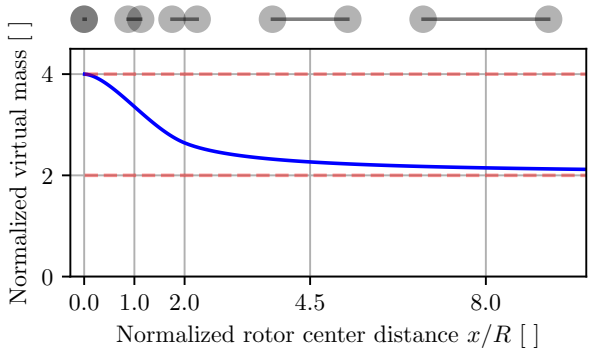

Figure 1: The influence of rotor separation on the virtual mass.

2.4 Dimensionality Reduction

Compiling the equations for the kinetic energies gives us the energy factor

$$\eta = \frac{E_i}{E_r} = \frac{\rho\pi R^3 \boldsymbol{w}^\intercal \boldsymbol{M}\boldsymbol{w}}{\frac{J}{2}\boldsymbol{\omega}^\intercal\boldsymbol{\omega}}. \tag{18}$$

By employing dimensionless variables, the model can be readily generalized and scaled. To this end, we use the Tip Speed Ratio (TSR), λ, and induction factor, a, instead of the rotational and induced velocities, ω and w. Assuming a constant freestream wind velocity, w_0, to simplify the analysis, the substitutions become:

$$\omega = \lambda\frac{w_0}{R} \tag{19}$$

$$w = aw_0. \tag{20}$$

Substituting the dimensional variables in (18) gives the energy factor in the nondimensional form:

$$\eta = \frac{2\pi\rho R^\beta \boldsymbol{a}^\intercal \boldsymbol{M}\boldsymbol{a}}{\gamma^2\sigma\kappa\boldsymbol{\lambda}^\intercal\boldsymbol{\lambda}}. \tag{21}$$

Assuming that both a and λ are equal for all rotors, the expression simplifies to

$$\eta = \frac{2\pi\rho R^\beta a^2 \mathbf{1}^T \boldsymbol{M}\mathbf{1}}{\gamma^2\sigma\kappa\lambda^2}, \tag{22}$$

where $\mathbf{1}$ is an appropriately sized column vector of ones.

3 Parameters

The non-dimensional energy factor in (22) evaluated at the optimum where $\lambda = \Lambda$ depends on several parameters. Namely: ρ, β, Λ, γ, κ and σ. The following paragraphs will elaborate on the applicable values and ranges for these parameters.

Air Density The air density, ρ, is often assumed to be constant but actually varies significantly with the change in temperature. Using the ideal gas law for computing the atmospheric density as shown in Manwell et al. (2002) one finds that $\rho = 1.225\,\mathrm{kg\,m^{-3}}$ at sea level at a temperature of 15 °C and atmospheric pressure 101.325 kPa. At the same pressure, but with a temperature of −30 °C the density increases to $1.452\,\mathrm{kg\,m^{-3}}$, while at 30 °C the density decreases to $1.164\,\mathrm{kg\,m^{-3}}$.

Optimal Tip Speed Ratio The optimal tip speed ratio of a given turbine is dependent on its design. Generally, wind turbines have optimal operational tip speed ratios in the range

$$4 \leq \Lambda \leq 10 \tag{23}$$

Bakırcı and Yılmaz (2018), with typical values being around 7, which is also the case for the NREL 5MW reference turbine Jonkman et al. (2009).

Blade Mass Obtaining numerical values for the parameters describing the blade mass, κ and β, was performed by minimizing the error of a normalized least squares fit with empirical data. The data for commercial turbines was aggregated from Ashwill (2006), Griffith and Richards (2014), and Crawford (2011), while data for small turbines was taken from More and Roy (2020) and Istabreeze (2023). The normalization is crucial for a fair fit, as smaller and lighter blades effectively would otherwise have been ignored. The optimization process yielded $\kappa = 3.1$ and $\beta = 0.6$. Figure 2 shows the data points and the resulting model. Additionally, keeping one of the parameters at the optimal solution, the other was adjusted to give a lower and upper bound, as shown in the figure.

Blade Inertia Wind turbine blades have a nonhomogeneous mass distribution along the blade due to various factors such as chord length and material composition. While the radius of gyration for a pipe with homogeneous mass distribution is $\sqrt{1/3}$, it is expected that a wind turbine blade will have a somewhat smaller radius of gyration, since the mass is concentrated at the blade root. Using data from Rinker and Dykes (2018) and Jonkman et al. (2009), a minimum value of

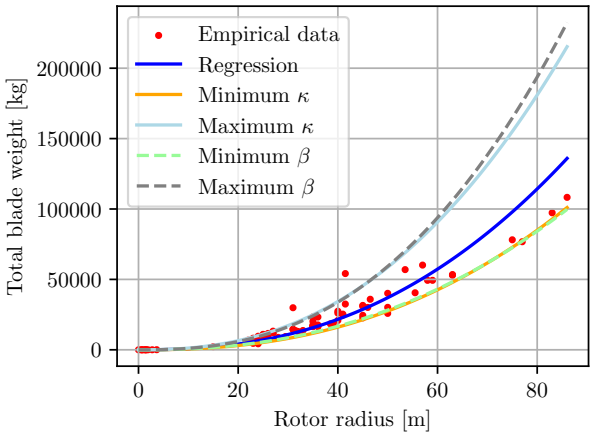

Figure 2: Rotor masses and the corresponding weights.

0.406 and a maximum of 0.413 was found. We adopt $\gamma = \sqrt{1/6} \approx 0.408$ as a representable value being within the range of empirical data and representing half the value of a homogeneously distributed mass.

Rotor Inertia The relation between the blade and rotor inertia, σ, was found using data from Rinker and Dykes (2018). While the values typically were around $\sigma = 1.19$, a minimum of 1.13 and maximum of 1.23 were also observed.

Table 1 shows a summary of all the parameters and their ranges, with the minimum, typical and maximum values.

Table 1: Modeling parameters and their respective ranges.

Parameter	Unit	Min.	Typ.	Max.
ρ	$\mathrm{kg\,m^{-3}}$	1.164	1.224	1.452
Λ	-	4	7	10
κ	$\mathrm{kg\,m^{3\text{-}\beta}}$	2.3	3.1	4.9
β	-	0.48	0.6	0.67
γ	-	0.406	0.408	0.413
σ	-	1.13	1.19	1.23

4 Energy Analysis

We can now analyze the energy factor from (22) for various rotor sizes and configurations. Figure 3 shows the various setups considered, ranging from 1 to 109 rotors congregated in a hexagonal grid and shaped to resemble a circle. The total swept area, and total power, are the same for all four configurations.

Let R_E denote the equivalent single rotor radius required to obtain a desired total swept area, and total power, with N rotors. The individual rotor radius for each of the N rotors is given by

$$R = \frac{R_E}{\sqrt{N}}. \tag{24}$$

Inserting (24) and the proportionality

$$\mathbf{1}^T \boldsymbol{M} \mathbf{1} = \alpha N^{3/2}\,, \quad N \geq 4. \tag{25}$$

into (22) we get

$$\eta_N = \frac{2\pi\rho R_E^{\beta} a^2 \alpha N^{(3-\beta)/2}}{\gamma^2 \sigma \kappa \lambda^2}\,, \quad N \geq 4. \tag{26}$$

Comparing the energy factors for the single and multirotor cases gives the relation

$$\frac{\eta_N}{\eta} = \frac{\alpha}{\mu} N^{(3-\beta)/2}\,, \quad N \geq 4. \tag{27}$$

Ideally, α would equal μ, however, when computing α for the given multirotor setup, one finds that $\alpha \approx 0.808$, which is slightly smaller than μ. Since (27) is strictly positive, it is clear that the energy in the induced flow in a multirotor system is always greater than that of a mono-rotor system with similar dimensions. Examining (26), one can see that the term $N^{(3-\beta)/2}$ is responsible for the changes due to the multirotor setup, the multirotor effect. Within the range of numerical values for β, the multirotor effect is positive with slightly faster than linear growth.

Inserting the values from Table 1 into (22) we obtain the energy factor for the given system as a function of the radius. Table 2 summarizes the energy factors for three different system sizes and four different configurations, varying from 1 to 109 rotors as shown in Figure 3.

Table 2: Energy factors for different multirotor setups

Equivalent	η for different values of N [ ]			
radius [m]	$N = 1$	$N = 7$	$N = 19$	$N = 109$
63	0.29	2.9	9.4	76
25	0.17	1.6	5.4	44
1.1	0.026	0.25	0.83	6.8

The energy factors for the 5 MW NREL reference turbine presented in Jonkman et al. (2009) with $R = 63\,\mathrm{m}$ and swept area of $12\,468\,\mathrm{m}^2$ is given in the first numerical row of Table 2. In the single rotor case we have that $\eta = 0.29$, Meaning that the rotor contains about three times more energy than the inflow. While

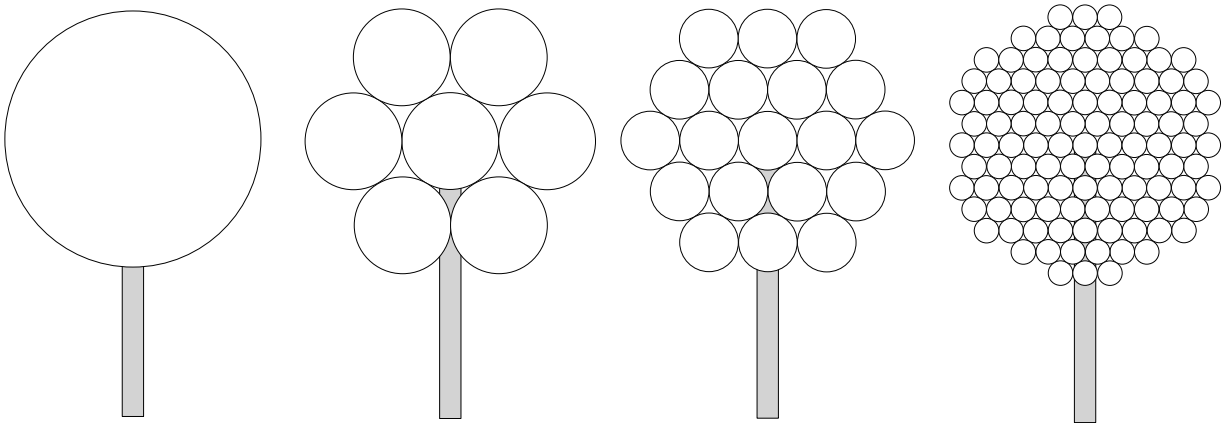

(a) 1 rotor. (b) 7 rotors. (c) 19 rotors. (d) 109 rotors.

Figure 3: Example setups of multirotor turbines with varying rotor counts.

the rotor contains significantly more energy, the inflow still represents one quarter of the total energy. Increasing the rotor count, i.e. changing out one large rotor for several smaller ones results in an increased energy factor. In fact, with 109 rotors of radius $\approx 6\,\mathrm{m}$, the energy factor is as large as 76, indicating that almost all the energy is stored in the induced flow.

The second numerical row in Table 2 shows the 750 kW wind turbine presented in Rinker and Dykes (2018), for which the same trends as the 5 MW turbine can be observed.

Finally, the last row shows the 1 kW wind turbine from Istabreeze (2023), with an energy factor of 0.026 in the single rotor case, rendering the inflow insignificant from an energy perspective. However, a multirotor setup with only 7 rotors already makes the inflow a significant shareholder of the total energy.

Worth noting is that we get an increasing energy factor with increasing rotor radius. In other words, for larger rotor radii, a larger proportion of the total energy is present in the induced flow. Likewise, for small rotor radii, almost all energy is stored in the rotor. This effect arises because the rotors in larger wind turbines are proportionally lighter than they theoretically should be, since $\beta > 0$.

Considering a slightly different application, namely remote-controlled helicopters or drones, these will typically experience energy factors between 0.01 and 0.00003, highlighting that in such systems, the energy is almost exclusively stored in the rotors.

Another conceptually similar system is subsea or tidal turbines. These systems operate in a fluid about 1000 times denser than the atmosphere. Consequently, the energy factor becomes 1000 times greater, implying that a substantially larger part of the energy is stored in the inflow.

5 Dynamics

The previous energy analysis has illustrated the relative importance of dynamic inflow in rotor systems in terms of kinetic energy. The kinetic energy of a system is closely coupled to the system dynamics, which will now be investigated.

5.1 Rotor

Using Newton's second law for rotational motion, the dynamics of the rotational velocity of a wind turbine can be expressed as

$$J\dot{\boldsymbol{\omega}} = \boldsymbol{q} - \boldsymbol{q}_g, \tag{28}$$

where $\boldsymbol{q}$ and $\boldsymbol{q}_g$ are vectors containing all rotor and generator torques, respectively. The generator torques are considered the main control inputs of a wind turbine. While some turbines also have the possibility of controlling the blade pitch, this is not considered relevant in the present work. Various control algorithms for computing the generator torque exist, see Novaes Menezes et al. (2018) for a review. Assuming we are close to the optimum, which generally should be the case for wind turbines during operation, we approximate any control algorithm by the Maximum Power Point Tracking (MPPT) algorithm for optimal torque control,

$$\boldsymbol{q}_g = \frac{1}{2}\rho\pi R^2 C_p \left(\frac{R}{\Lambda}\right)^3 \boldsymbol{\omega}^2. \tag{29}$$

In the MPPT algorithm, C_p denotes the optimal power coefficient and Λ the corresponding optimal TSR. From central results in momentum theory, the well-known Betz limit gives $C_p = 16/27$. The value of the optimal TSR will depend on the particular blade design used.

Inserting for the generator torque (29) and inertia (4) into (28) and making it dimensionless using (19) and (20), one obtains

$$\dot{\boldsymbol{\lambda}}\kappa\sigma w_0^2\gamma^2 R^{3-\beta} = \boldsymbol{q} - \frac{\pi C_p \rho R^3 w_0^2}{2\Lambda^3}\boldsymbol{\lambda}^2. \tag{30}$$

5.2 Inflow

The inflow dynamics in the multirotor case are not decoupled as is the case for the rotor dynamics. While modeling multirotor inflow dynamics is a complex topic in and of itself, we can use a shortcut by noting that the mass m in the typical formula for kinetic energy

$$E_k = \frac{1}{2}mv^2 \tag{31}$$

for a system with velocity v, is the same mass that enters the linear dynamic equation for the same system

$$m\dot{v} = \tau - vk, \tag{32}$$

where τ is some forcing and k a dimensional constant making kv the same units as τ. Using the notion of a virtual mass for the induced flow, we have from (14) that

$$\boldsymbol{M}_v = 2\rho\pi R^3 \boldsymbol{M}. \tag{33}$$

We thus propose that a simple approximation to the axial multirotor dynamic inflow on coplanar actuator disks can be modeled with

$$\boldsymbol{M}_v\dot{\boldsymbol{w}} = \boldsymbol{f} - 2\pi\rho R^2 \boldsymbol{w}\left|w_0 - \boldsymbol{w}\right|, \tag{34}$$

where $\boldsymbol{f}$ and $\boldsymbol{a}$ are vectors containing the thrust and induction factors for each rotor, respectively. In dimensionless form the dynamics become

$$\boldsymbol{M}\dot{\boldsymbol{a}} = \frac{\boldsymbol{f}}{2\pi\rho R^2 w_0^2} - \boldsymbol{a}\left|1 - \boldsymbol{a}\right|. \tag{35}$$

For a single rotor, we get

$$\mu\dot{\boldsymbol{a}} = \frac{\boldsymbol{f}}{2\pi\rho R^2 w_0^2} - \boldsymbol{a}\left|1 - \boldsymbol{a}\right|, \tag{36}$$

which is a dimensionless variant of the model for mean axial flow given in Peters (2009).

5.3 Airloads

A crucial part of wind turbine systems are the airloads, which allow for the transformation of kinetic energy in the wind to mechanical energy in the rotor. We will now present a simple model for the required airloads, namely the thrust f and torque q.

When the rotor blade is subjected to a relative fluid flow, forces and moments are generated. Since the aerodynamics are passive, i.e. no energy is generated, we know that

$$fw = q\omega. \tag{37}$$

Furthermore, it is known that the power is given in terms of velocities cubed multiplied by a constant k. The primal solution to (37) is thus

$$f = kw\omega \tag{38}$$

$$q = kw^2. \tag{39}$$

The constant k is found by using (36) in steady state at the optimum $a = 1/3$:

$$k = \frac{2\pi\rho R^3}{3\lambda}. \tag{40}$$

Making the airloads dimensionless using

$$d\omega = d\lambda\left(\frac{w_0}{R}\right)^2 \tag{41}$$

$$dw = da\frac{w_0^2}{R} \tag{42}$$

and inserting them into (36) and (30) yields

$$\boldsymbol{M}\dot{\boldsymbol{a}} = \frac{\lambda(1-\boldsymbol{a})}{3\Lambda} - \boldsymbol{a}\left|1-\boldsymbol{a}\right| \tag{43}$$

$$\dot{\boldsymbol{\lambda}}\kappa\sigma\gamma^2 R^{3-\beta} = \frac{2\pi(1-\boldsymbol{a})^2\rho R^3}{3\Lambda} - \frac{8\pi\boldsymbol{\lambda}^2\rho R^3}{27\Lambda^3}. \tag{44}$$

6 Linearization and System Analysis

The model formulation in (43) and (44) is not directly tractable for further analysis. However, analyzing the system behavior for small perturbations around the optimum can easily be achieved. This allows a simplified system analysis around the equilibrium of the system.

Wind turbines typically operate around their optimum, where momentum theory gives that $a = 1/3$, and $\lambda = \Lambda$. A first-order Taylor series expansion around the optimum approximates the behavior in the form of a Linear Time-Invariant (LTI) system given by:

$$\begin{bmatrix}\dot{\boldsymbol{\lambda}}\\ \dot{\boldsymbol{a}}\end{bmatrix} = \begin{bmatrix}-\frac{8}{3}\bar{\boldsymbol{\eta}}\boldsymbol{M}^{-1} & -4\Lambda\bar{\boldsymbol{\eta}}\boldsymbol{M}^{-1}\\ \frac{2}{9\Lambda}\boldsymbol{M}^{-1} & -\frac{2}{3}\boldsymbol{M}^{-1}\end{bmatrix}\begin{bmatrix}\Delta\boldsymbol{\lambda}\\ \Delta\boldsymbol{a}\end{bmatrix} = \boldsymbol{A}\begin{bmatrix}\Delta\boldsymbol{\lambda}\\ \Delta\boldsymbol{a}\end{bmatrix} \tag{45}$$

where the power factor at the equilibrium

$$\bar{\boldsymbol{\eta}} = \frac{2\pi\rho R^\beta}{9\gamma^2\kappa\Lambda^2\sigma}\boldsymbol{M} \tag{46}$$

plays a central role. The matrix $\boldsymbol{A}$ characterizes the LTI system where $\Delta\boldsymbol{\lambda} = \boldsymbol{\lambda} - \Lambda$ and $\Delta\boldsymbol{a} = \boldsymbol{a} - 1/3$ describe perturbations from the equilibrium.

An analysis of the system's response for small perturbations in $\boldsymbol{a}$ and $\boldsymbol{\lambda}$ can now be performed. Such an analysis makes it possible to understand how the nonlinear system behaves around the optimum for varying rotor radii and multirotor configurations. A useful approach for LTI systems is to examine the eigenvalues of the system matrix, $\boldsymbol{A}$. For the model parameters, we will use their typical values as presented in Table 1.

While the system formulation in (45) is given in its dimensionless form, the system can easily be made dimensional by inserting the dimensional variables from (19) and (20). In the following, the eigenvalues and time constants will be dimensional with $w_0 = 10\,\mathrm{m\,s^{-1}}$ and varying R.

6.1 Eigenvalues

While the general eigenvalues in the multirotor case are difficult to analyze due to their quantity, we can make some interesting observations for the single-rotor case. With only one rotor, $\boldsymbol{A}$ becomes a 2×2 matrix with eigenvalues

$$\begin{bmatrix} -\frac{w_0}{R}\frac{1+4\bar{\eta}+\sqrt{16(\bar{\eta}-1)\bar{\eta}+1}}{3\mu} \\ \frac{w_0}{R}\frac{-1-4\bar{\eta}+\sqrt{16(\bar{\eta}-4)\bar{\eta}+1}}{3\mu}. \end{bmatrix} \tag{47}$$

The eigenvalues evaluate to either two unique real values or a complex conjugated pair, as shown in Figure 4.

From a stability perspective, Figure 4 confirms that the real parts of the eigenvalues are negative, indicative of a stable system. However, it is notable that the eigenvalues become very small as the radius increases, indicating marginal stability for very large radii.

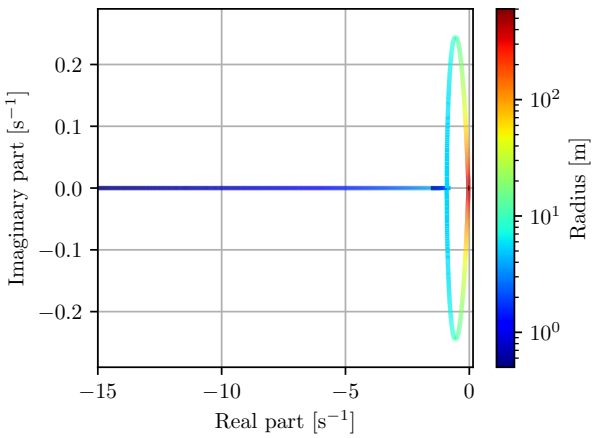

Figure 4: Eigenvalues of linearized single rotor wind turbine system at equilibrium.

The presence of the complex conjugate pair is confined to the region where

$$\left(2-\sqrt{3}\right) \leq 4\eta \leq \left(2+\sqrt{3}\right), \tag{48}$$

which, for the present parameters becomes approximately $5.48\,\mathrm{m} < R < 442\,\mathrm{m}$. In this expression, the exponent correction of the mass scaling law, β, is pivotal; omitting it, i.e. $\beta = 0$, precludes the existence of the complex conjugated eigenvalue pair. Practically, this suggests that the appearance of complex conjugated eigenvalues is caused by wind turbine blades being lighter than predicted by theoretical scaling laws, resulting in a possibly underdamped system.

For small wind turbines with $R < 5.48\,\mathrm{m}$ the system has two distinct real negative eigenvalues, suggesting the system is overdamped with no oscillations.

6.2 Time Constants

A slightly modified version of the eigenvalues, namely the time constants, can give an intuitive interpretation of the system for both single and multirotor setups.

Analyzing the time constants' dependence on both the radius and rotor count in the general case is challenging. For this reason, the dependence on the radius and rotor count will be analyzed separately, whilst an example for varying rotor sizes and counts will be shown for the cases presented in Table 2.

The system time constants represent the coupled dynamics of the wind turbine at the equilibrium. However, the time constant for the inflow without rotor dynamics can be found at the limit where $\gamma \to 0$. Likewise, the time constant for only the rotor dynamics can be found by computing the limit as $\mu \to 0$.

Figure 5 shows the time constants for systems with varying rotor radius for two values of β. The case where $\beta = 0$ is shown in Figure 5a. Here, the time constants scale linearly with system size, and the rotor mass scales according to the cube law.

The time constants for the model with $\beta = 0.6$, which based on the preceding discussion is the typical value, are shown in Figure 5b. As β increases, the rotor mass and thus moment of inertia is proportionally lower than the cube law would suggest. This decreases the time constants for the rotor relative to the case where $\beta = 0$ and consequently, the whole system as the radius increases. It follows from this, that blades with $R < 1$ get a proportionally higher inertia due to their proportionally large mass.

Overall, the time constants are reasonably alike for small to intermediate radii. More specifically, it seems like the rotor dynamics are dominating up until about $R = 40\,\mathrm{m}$, after which the inflow dynamics take over. This analysis is useful for deciding what components need to be included for proper wind turbine simulation and control problems. The results show that for small rotor radii, the rotor is slow compared to the inflow, while the opposite is true for large wind turbines, where the inflow is deciding.

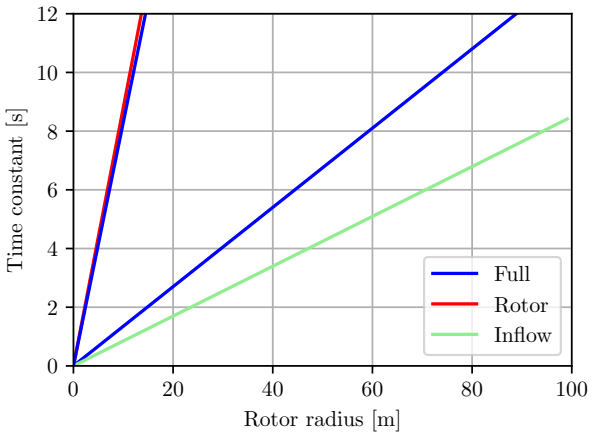

(a) $\beta = 0.0$

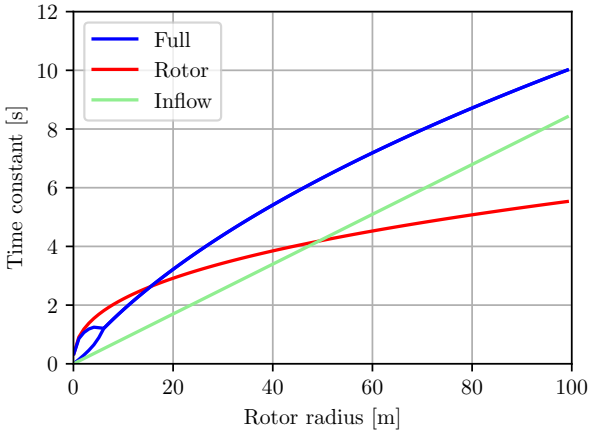

(b) $\beta = 0.6$

Figure 5: Time constants for system setups.

In contrast to the single-rotor case, the multirotor system includes the coupling between the rotors due to the aerodynamic interaction caused by the induced flow. As with the energy factor, this coupling scales with the amount of rotors present in the system. Figure 6 shows how the smallest and largest time constants of a multirotor system change for varying rotor counts for a system constant rotor radius $R = 30\,\mathrm{m}$ stacked in a circular hexagonal pattern, as illustrated in Figure 3. Importantly, the time constants are strictly positive, meaning that the underlying system is stable.

As one can see in Figure 6, the smallest time constant decreases in the beginning but stays reasonably constant as the rotor count increases. This might be because the high-frequency behavior is concentrated in clusters around each rotor, meaning that adding more rotors far away does not change the local behavior of each rotor. On the other hand, the largest time constant represents the slowest behavior of the system, which is expected to grow with the system size as there

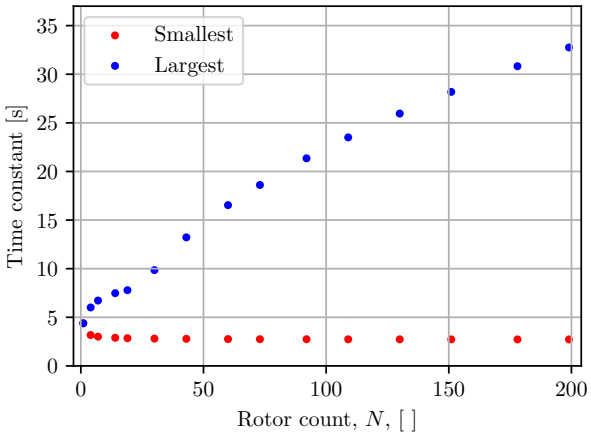

Figure 6: Largest and smallest time constants for multirotor setup with $R = 30\,\mathrm{m}$.

effectively is more mass to move.

Finally, we will consider the case where we have a given total swept area, and examine how substituting one large rotor for several smaller ones with in total the same swept area influences the system dynamics. We will here use the same setups as shown in Figure 3 and discussed in Table 2. The smallest and largest eigenvalues for the different wind turbine system configurations are shown in Table 3.

As one can see in Table 3, the smallest time constant becomes slightly smaller as the rotor count increases and consequently the rotor size decreases. The opposite goes for the largest time constant, as it increases significantly. A multirotor system will thus have both quicker and slower dynamics than those of an equivalently large single-rotor system. This is in contrast to the decoupled case, in which all time constants decrease with decreasing radius.

7 Conclusion

This work employed theoretical models with parameters tuned using theoretical results and empirical data to demonstrate how a wind turbine system is affected by the rotor size and quantity. These results have been analyzed in terms of system stability and they also give important insights into the requirements for simulation and control design.

Under the assumptions of actuator disks and strictly axial flow, key insights from our analysis include:

- Energy distribution:
  - Systems with large rotor radii store proportionally more energy in the inflow than systems with small rotor radii.

Table 3: Time constants for different multirotor setups

Equivalent radius [m]	Time constants for different values of N [s]							
	$N = 1$		$N = 7$		$N = 19$		$N = 109$	
	Min	Max	Min	Max	Min	Max	Min	Max
63	7.43	7.43	5.43	10.3	5.18	18.8	5.0	51.3
25	3.82	3.82	2.59	6.01	2.45	7.04	2.35	19.3
1.1	0.15	0.86	0.08	0.89	0.07	0.89	0.07	1.39

  - Systems with multiple rotors store more energy in the inflow than an equivalent single-rotor system.

- Stability:
  - Systems with large rotor radii exhibit marginal stability.
  - Increasing the rotor count generates eigenvalues that are both less and more stable.

- Dynamics:
  - Single rotor systems with $R > 49\,\text{m}$ are primarily governed by the inflow dynamics.
  - Single rotor systems with $R < 49\,\text{m}$ are primarily governed by the rotor dynamics.
  - Multirotor systems with large rotor counts are primarily governed by the inflow dynamics.

These results highlight the importance of including dynamic inflow in wind turbine control and modeling. This becomes more important as the turbines get larger in rotor radius or when they get arranged in multi-rotor configurations. These findings agree well with and elaborate on results from previous work, Henriksen et al. (2013, 2012); Odgaaard et al. (2015).

Concluding, this study has shown that dynamic inflow is necessary in almost all wind turbine systems. The only case in which the dynamic inflow might be omitted without affecting model validity is for systems with very small and few rotors, such as small remote-controlled helicopters.

References

Ashwill, T. Blade Technology Innovations for Utility-Scale Turbines. 2006.

Bakırcı, M. and Yılmaz, S. Theoretical and computational investigations of the optimal tip-speed ratio of horizontal-axis wind turbines. *Engineering Science and Technology, an International Journal*, 2018. 21(6):1128–1142. doi:https://doi.org/10.1016/j.jestch.2018.05.006.

Bashetty, S. and Ozcelik, S. Review on dynamics of offshore floating wind turbine platforms. *Energies*, 2021. 14(19). doi:10.3390/en14196026.

Batchelor, G. K. *An introduction to fluid dynamics*. Cambridge mathematical library. Cambridge University Press, Cambridge, 1967.

Canet, H., Bortolotti, P., and Bottasso, C. L. On the scaling of wind turbine rotors. *Wind Energy Science*, 2021. 6(3):601–626. doi:10.5194/wes-6-601-2021.

Conway, J. T. Analytical solutions for the actuator disk with variable radial distribution of load. *Journal of Fluid Mechanics*, 1995. 297:327–355. doi:10.1017/S0022112095003120.

Crawford, C. A. The Path From Functional to Detailed Design of a Coning Rotor Wind Turbine Concept. *Proceedings of the Canadian Engineering Education Association (CEEA)*, 2011. doi:10.24908/pceea.v0i0.3768.

Griffith, D. and Richards, P. The SNL100-03 Blade: Design Studies with Flatback Airfoils for the Sandia 100-meter Blade. Technical Report SAND2014-18129, 1159116, 537751, 2014.

Henriksen, L., Hansen, M., and Poulsen, N. Beyond the cp-curve in model-based control of wind turbines. *European Wind Energy Conference and Exhibition 2012, EWEC 2012*, 2012. 1:143–152.

Henriksen, L. C., Hansen, M. H., and Poulsen, N. K. A simplified dynamic inflow model and its effect on the performance of free mean wind speed estimation. *Wind Energy*, 2013. 16(8):1213–1224. doi:https://doi.org/10.1002/we.1548.

Hutchinson, M. and Zhao, F. Global wind report 2023. Technical report, 2023. URL

https://gwec.net/wp-content/uploads/2023/03/GWR-2023_interactive.pdf.

Istabreeze. Blades of wind generators. https://istabreeze.us/wind-generators-accessories/blades-of-wind-generators/, 2023. [Online; accessed 10-October-2023].

Johnson, K., Pao, L., Balas, M., and Fingersh, L. Control of variable-speed wind turbines: standard and adaptive techniques for maximizing energy capture. *IEEE Control Systems Magazine*, 2006. 26(3):70–81. doi:10.1109/MCS.2006.1636311.

Jonkman, J., Butterfield, S., Musial, W., and Scott, G. Definition of a 5MW reference wind turbine for offshore system development. Technical report, National Renewable Energy Laboratory (NREL), 2009.

Mancini, S., Boorsma, K., Schepers, G., and Savenije, F. A comparison of dynamic inflow models for the blade element momentum method. *Wind Energy Science*, 2023. 8(2):193–210. doi:10.5194/wes-8-193-2023.

Manwell, J., McGowan, J., and Rogers, A. *Wind Energy Explained*. John Wiley & Sons, Ltd, Chichester, UK, 2002. doi:10.1002/0470846127.

More, A. and Roy, A. Design and Weight Minimization of Small Wind Turbine Blade for Operation in Low-Wind Areas. In S. Singh and V. Ramadesigan, editors, *Advances in Energy Research, Vol. 2*, pages 311–322. Springer Singapore, Singapore, 2020. doi:10.1007/978-981-15-2662-6_29. Series Title: Springer Proceedings in Energy.

Novaes Menezes, E. J., Araújo, A. M., and Bouchonneau da Silva, N. S. A review on wind turbine control and its associated methods. *Journal of Cleaner Production*, 2018. 174:945–953. doi:https://doi.org/10.1016/j.jclepro.2017.10.297.

Odgaaard, P. F., Knudsen, T., Overgaard, A., Steffensen, H., and Jørgensen, M. Importance of dynamic inflow in model predictive control of wind turbines. *IFAC-PapersOnLine*, 2015. 48(30):90–95. doi:https://doi.org/10.1016/j.ifacol.2015.12.359. 9th IFAC Symposium on Control of Power and Energy Systems CPES 2015.

Pao, L. Y. and Johnson, K. E. A tutorial on the dynamics and control of wind turbines and wind farms. In *2009 American Control Conference*. pages 2076–2089, 2009. doi:10.1109/ACC.2009.5160195.

Papi, F., Jonkman, J., Robertson, A., and Bianchini, A. Going beyond bem with bem: an insight into dynamic inflow effects on floating wind turbines. *Wind Energy Science Discussions*, 2023. 2023:1–29. doi:10.5194/wes-2023-109.

Peters, D. A. How dynamic inflow survives in the competitive world of rotorcraft aerodynamics. *Journal of the American Helicopter Society*, 2009. 54(1).

Rinker, J. and Dykes, K. WindPACT Reference Wind Turbines. Technical Report NREL/TP–5000-67667, 1432194, 2018.

Tang, C., Pathmanathan, M., Soong, W. L., and Ertugrul, N. Effects of Inertia on Dynamic Performance of Wind Turbines. *Australasian Universities Power Engineering Conference*, 2008.

Veers, P., Bottasso, C. L., Manuel, L., Naughton, J., Pao, L., Paquette, J., Robertson, A., Robinson, M., Ananthan, S., Barlas, T., Bianchini, A., Bredmose, H., Horcas, S. G., Keller, J., Madsen, H. A., Manwell, J., Moriarty, P., Nolet, S., and Rinker, J. Grand challenges in the design, manufacture, and operation of future wind turbine systems. *Wind Energy Science*, 2023. 8(7):1071–1131. doi:10.5194/wes-8-1071-2023.

Zhang, Y., Cai, X., Lin, S., Wang, Y., and Guo, X. Cfd simulation of co-planar multi-rotor wind turbine aerodynamic performance based on alm method. *Energies*, 2022. 15(17). doi:10.3390/en15176422.